The Visualization and Measurement of Left Ventricular Deformation using Finite Element Models

Burkhard Wünsche[a] and Alistair A. Young[b]

[a]Department of Computer Science, University of Auckland, Private Bag 92019, Auckland, New Zealand, email: burkhard@cs.auckland.ac.nz

[b]Department of Anatomy with Radiology, Department of Physiology, University of Auckland, Private Bag 92019, Auckland, New Zealand, email: a.young@auckland.ac.nz

Heart diseases cause considerable morbidity and the prognosis after heart failure is poor. An improved understanding of cardiac mechanics is necessary to advance the diagnosis and treatment of heart diseases. This article explains techniques for visualizing and evaluating biomedical finite element models and demonstrates their application to biomedical data sets by using as an example two models of a healthy and a diseased human left ventricle. The following contributions are made: we apply techniques traditionally used in solid mechanics and computational fluid dynamics to biomedical data and suggest some improvements and modifications. We obtain new insight into the mechanics of the healthy and diseased left ventricle and we facilitate the understanding of the complex deformation of the heart muscle by novel visualizations. Finally we also introduce in this process a toolkit designed for visualizing biomedical data sets.

1. Introduction

Heart diseases remain the biggest killer in the western world [1]. One or multiple heart diseases can result in heart failure, which is a clinical syndrome that arises when the heart is unable to pump sufficient blood to meet the metabolic needs of the body at normal filling pressures [2]. The goal of recording and visualizing cardiac data sets is to recognize and predict heart diseases.

The cardiac data set used in this work is a finite element model of the human left ventricle developed by Young et al. [3,4]. The deformation of the *myocardium* (heart muscle) is represented by the *strain tensor*. We use a visualization toolkit specifically designed for biomedical models [5,6] to visualize the strain tensor field and to evaluate the performance of a healthy and a diseased human left ventricle. The visualization techniques novel to this field are explained and the results are discussed and interpreted.

The first section of this paper explains notations and introduces the strain tensor and some of its properties. The next section gives an overview of cardiac diseases and explains why visualizing myocardial strain is important in their diagnosis and understanding. It follows an introduction of the FE model and the computation of cardiac performace measures from it. The subsequent sections explain the visualization toolkit and the visu-

alization of the left ventricular models. We conclude with a discussion of our results and mention avenues for future research.

1.1. Notations

As shown in figure 1 (a) the heart consists of two main chambers, the left and the right ventricle. When discussing the heart it is convenient to introduce names for the different regions of the *myocardium* (heart muscle). Figure 1 (b) illustrates that the myocardium of the left ventricle is divided in circumferential direction into a *septal*, *anterior*, *lateral*, and *inferior* (or *posterior*) region. The anterior side of the left ventricle faces the chest, the inferior (posterior) side faces the back, and the septal region represents the interventricular septum which separates the two ventricles. In longitudinal direction the left ventricle is divided into an *apical*, a *mid-ventricular* or *equatorial*, and a *basal* region [7]. Finally in radial direction the myocardium is divided into a *subepicardial*, *subendocardial*, and *midmyocardial* region. The terms refer to the parts of the myocardium neighbouring the *epicardial surface* (the outer layer of the heart muscle), the *endocardial surface* (the layer lining the ventricular cavity), and the region between them, respectively.

Other segmentations and nomenclatures have been suggested for different imaging modalities based on the practical clinical applications and the strengths and weaknesses of each imaging technique [8].

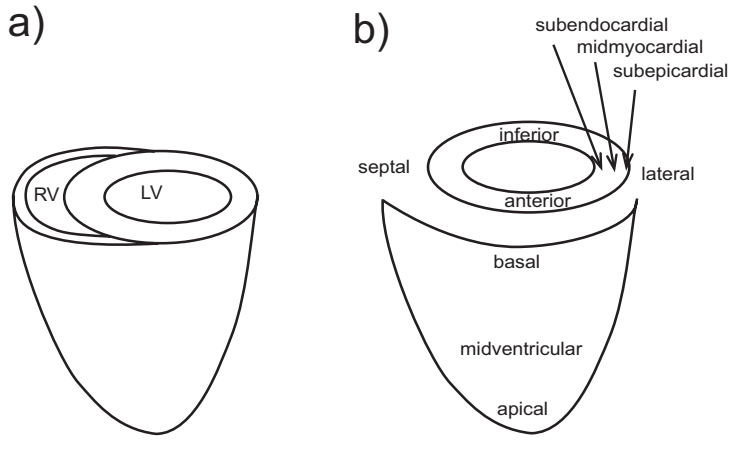

Figure 1. (a) Schematic drawing of the heart with the left (LV) and the right (RV) ventricle being indicated. (b) Illustration of the regions of the left-ventricular myocardium.

The contraction of the heart is called *systole* and the expansion *diastole*. The moment of maximum contraction of the left ventricle is called (left-ventricular) *end-systole* and the moment of maximum expansion is called (left-ventricular) *end-diastole* [4].

1.2. Displacement and Strain

The deformation of the heart can be described by a strain tensor field. In order to derive this measure first consider how an elastic body under an applied load deforms into

a new shape.

The theory of elasticity provides a mathematical description for the displacement the body undergoes. Figure 2 indicates a three-dimensional body before and after deformation. Under deformation the points P and Q move to position $\mathbf{x}' = \mathbf{x} + \mathbf{u}(\mathbf{x})$ and $\mathbf{x}' + d\mathbf{x}' = \mathbf{x} + d\mathbf{x} + \mathbf{u}(\mathbf{x} + d\mathbf{x})$, respectively, where $\mathbf{u}$ is called the *displacement field*.

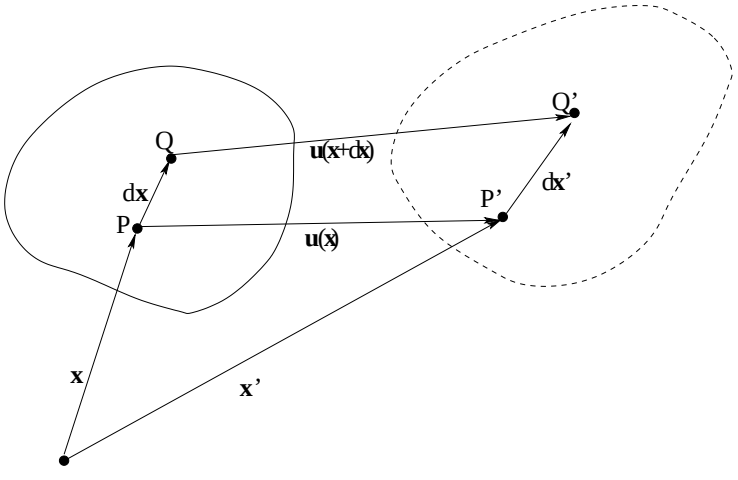

Figure 2. A body before and after deformation

If the points are only an infinitesimal distance apart the distance between the deformed points

$$d\mathbf{x}' = d\mathbf{x} + \mathbf{u}(\mathbf{x} + d\mathbf{x}) - \mathbf{u}(\mathbf{x}) \tag{1}$$

can be written as [9]

$$d\mathbf{x}' = d\mathbf{x} + (\nabla \mathbf{u}) d\mathbf{x} \tag{2}$$

where the second-order tensor

$$\nabla \mathbf{u} = \begin{pmatrix} \frac{\partial u_1}{\partial x_1} & \frac{\partial u_1}{\partial x_2} & \frac{\partial u_1}{\partial x_3} \\ \frac{\partial u_2}{\partial x_1} & \frac{\partial u_2}{\partial x_2} & \frac{\partial u_2}{\partial x_3} \\ \frac{\partial u_3}{\partial x_1} & \frac{\partial u_3}{\partial x_2} & \frac{\partial u_3}{\partial x_3} \end{pmatrix} \tag{3}$$

is known as the *displacement gradient*.

It can be seen that if $\nabla \mathbf{u} = \mathbf{0}$ then $d\mathbf{x}' = d\mathbf{x}$ and the motion in the neighborhood of point P is that of a rigid body translation. The information about the material deformation around P is contained in $\nabla \mathbf{u}$. It is desirable to define an entity which contains only information about deformation, but not about rotation. To do this consider two material vectors $d\mathbf{x}_1$ and $d\mathbf{x}_2$ issuing from point P. Their dot product after transformation is [9]

$$d\mathbf{x}_1'^T d\mathbf{x}_2' = d\mathbf{x}_1^T d\mathbf{x}_2 + 2 d\mathbf{x}_1^T \mathbf{E} d\mathbf{x}_2 \tag{4}$$

where the symmetric second-order tensor

$$\mathbf{E} = \frac{1}{2}\left((\nabla\mathbf{u}) + (\nabla\mathbf{u})^T + (\nabla\mathbf{u})^T(\nabla\mathbf{u})\right) \tag{5}$$

is the *Lagrangian strain tensor*. Note that if $\mathbf{E} = 0$ the lengths and angles between the material vectors $d\mathbf{x}_1$ and $d\mathbf{x}_2$ remain unchanged, i.e., the deformation $\nabla\mathbf{u}$ around point P is an infinitesimal rigid body rotation.

Since the strain tensor $\mathbf{E}$ is symmetric there always exist 3 *eigenvalues* λ_i and 3 mutually perpendicular *eigenvectors* $\mathbf{v}_i$ such that [9]

$$\mathbf{E}\mathbf{v}_i = \lambda_i\mathbf{v}_i \quad i = 1, 2, 3 \tag{6}$$

The eigenvectors $\mathbf{v}_1$, $\mathbf{v}_2$, and $\mathbf{v}_3$ of $\mathbf{E}$ are the *principal directions* of the strain, i.e., the directions in which there is no shear strain. The eigenvalues λ_1, λ_2, and λ_3 are the *principal strains* and give the unit elongations in the principal directions. The maximum, medium, and minimum eigenvalue are called the *maximum, medium, and minimum principal strain*, respectively.

2. Heart Failure

Causes of heart failure are differentiated into mechanical, myocardial, and rhythmic abnormalities [2]. Mechanical abnormalities include increased pressure or volume load (e.g., due to a dysfunctional valve) and bulging of the heart wall (ventricular aneurysm). Myocardial abnormalities include metabolic disorders (e.g., diabetes), inflammation, and *ischemia* (blockage of the coronary artery). Abnormalities of the cardiac rhythm or conduction disturbances include standstill, irregular heart beat (*fibrillation*), and abnormally rapid heart beat (*tachycardia*).

The most common fatal heart disease is *myocardial infarction* (heart attack), which occurs when a coronary artery is completely blocked (*stenosis*) and an area of the heart muscle dies because it is completely deprived of oxygen for an extended period of time. Acute myocardial infarction starts in the subendocardium and spreads to the subepicardium within 20-40 minutes after occlusion of the coronary artery [10]. Permanently damaged muscle is replaced by scar tissue, which does not contract like healthy heart tissue, and sometimes becomes very thin and bulges during each heart beat (*aneurysm*) [11,2].

The analysis of myocardial function is important for the diagnosis of heart diseases, the planning of therapy [10] and the understanding of the effect of cardiac drugs on regional function [12].

Many cardiac disorders result in regionally altered myocardial mechanics. Traditionally an abnormal contractile function of the ventricles has been determined by measuring the wall thickening using cine MRI images, Echocardiography [13,2,14,15] and SPECT [2]. Reported wall thickening rates during systole for a healthy heart vary from 40% [16] to 80% [17]. Detectable abnormalities include reduced wall thickening after myocardial infarction [17], regional wall thinning of an infarcted area and compensatory wall thickening and hypertrophy, and left ventricular enlargement (remodelling) [2, pp.648].

Wall thickening, however, is only one indicator of impending heart failure and other motion dependent indicators have been reported in the literature [18–20,11]. A full description of the deformation behaviour of the myocardium is therefore desirable. The

previous section demonstrated that such a description is given by the strain tensor field **E** which is mathematical represented by a 3×3 matrix.

2.1. Myocardial Strain as an Indicator of Heart Failure

The concept of myocardial strain and stress estimation was originally introduced by Mirsky and Parmley [21]. Strain is defined as the pure deformation (without translation and rotation). Scalar strain values can be derived from the strain tensor to quantify the length change of an infinitesimal material volume in a given direction (e.g., the circumferential or radial direction of the ventricle). Negative strain values are interpreted as a local shortening of the myocardium and positive strain values as a local elongation.

Although it is possible to directly measure regional myocardial strain (see subsection 3.2), there is no method for directly measuring myocardial stress. Given the complex geometry, non-linear material properties, large deformations and complex tissue microstructure of the heart, regional stress can only be estimated by solving the equations of finite elasticity using the finite element method [22]. Note that the finite element model used in this paper to reconstruct motion and strain from the MR images can be directly used in the finite element method to solve for stress, motion and material properties. This computational analysis is outside the scope of the current paper.

Abnormalities in the myocardial strain are detectable before first symptoms of a heart attack occur [11] so that measuring and visualizing the strain might represent a useful diagnosis tool. Heimdal et al. report that the stress-strain relationship more selectively describes the overall tissue characteristics than the pressure-volume relationship [23]. McCulloch and Mazhari [22] suggest several possible roles of strain and stress measurement in clinical diagnosis.

3. A Left-Ventricular Finite Element Model

A model for reconstructing the 3D motion and strain of the left ventricle from tagged Magnetic Resonance Imaging images has been developed by Young et al. [24,25] based on a finite element model of the left ventricle.

The following two subsections describe the definition of the finite element geometry and introduce the left-ventricular model and the myocardial strain field used in this work.

3.1. Finite-Element Geometry

The geometry of a *finite element* model is described by a set of nodes and a set of elements, which have these nodes as vertices. The nodal coordinates are interpolated over an element using *interpolation functions*. Curvilinear elements can be defined by specifying nodal derivatives.

As an example of a finite element consider the cubic Hermite-linear Lagrange element in two dimensions shown in figure 3 (b). We first specify a parent element, shown in part (a) of the figure, which is a square in ξ-parameter space. The coordinates ξ_j ($0 \leq \xi_j \leq 1$, j=1,2) are called the element or *material coordinates*. The value of some variable u (e.g., temperature) at the material coordinates ξ is then specified by interpolating the variables u_i linearly in the given parameter direction. In our example we assume that additionally derivatives in ξ_1-direction $\left(\frac{\partial u}{\partial \xi_1}\right)_i$ $(i = 1, \ldots, 4)$ are specified at the element nodes. In this case a cubic Hermite interpolation is performed in that direction.

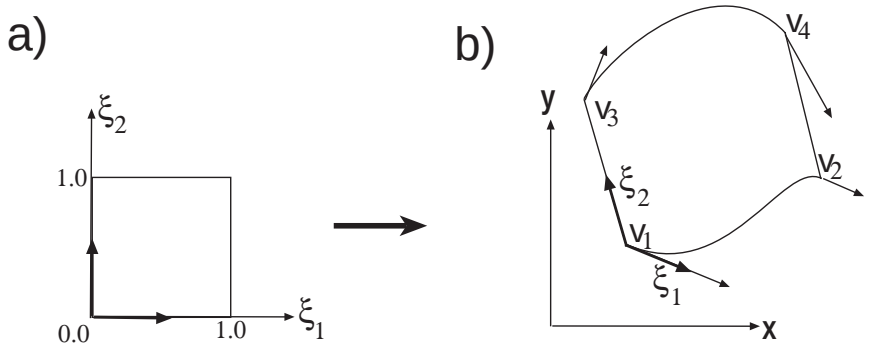

Figure 3. A cubic Hermite-linear Lagrange finite element with vertices v_i and vertex tangents in ξ_1 direction indicated by arrows.

The cubic Hermite-linear interpolation of u over the entire 2D parameter space is then defined by the tensor products of the interpolation functions in each parameter direction:

$$\begin{aligned} & u(\xi_1,\xi_2) = \\ & H_1^0(\xi_1)L_1(\xi_2)u_1 + H_2^0(\xi_1)L_1(\xi_2)u_2 \\ + \;& H_1^0(\xi_1)L_2(\xi_2)u_3 + H_2^0(\xi_1)L_2(\xi_2)u_4 \\ + \;& H_1^1(\xi_1)L_1(\xi_2)\left(\frac{\partial u}{\partial \xi_1}\right)_1 + H_2^1(\xi_1)L_1(\xi_2)\left(\frac{\partial u}{\partial \xi_1}\right)_2 \\ + \;& H_1^1(\xi_1)L_2(\xi_2)\left(\frac{\partial u}{\partial \xi_1}\right)_3 + H_2^1(\xi_1)L_2(\xi_2)\left(\frac{\partial u}{\partial \xi_1}\right)_4 \end{aligned} \tag{7}$$

where

$$L_1(\xi) = 1-\xi, \quad \text{and} \quad L_2(\xi) = \xi \tag{8}$$

are the one-dimensional linear Lagrange basis functions, and

$$\begin{aligned} & H_1^0(\xi) = 1-3\xi^2+2\xi^3, H_1^1(\xi) = \xi(\xi-1)^2 \\ & H_2^0(\xi) = \xi^2(3-2\xi), \quad H_2^1(\xi) = \xi^2(\xi-1) \end{aligned} \tag{9}$$

are the one-dimensional cubic Hermite basis functions.

The geometry of an element in world coordinates (figure 3 (b)) is obtained by specifying the world-coordinates $\mathbf{v}_i$ and the ξ_1-tangents $\left(\frac{\partial \mathbf{v}}{\partial \xi_1}\right)_i$ $(i = 1,\ldots,4)$ of the element vertices and interpolating them as above.

3.2. The Model of the Left Ventricle

The model geometry has been computed by tracking myocardial contours on tagged MRI slices and by fitting a surface through them using a prolate spheroidal coordinate system aligned to the central axis of the left ventricle [24,25]. The FE model is then created by placing nodes at equal angular intervals in the circumferential and longitudinal

direction and by fitting the radial coordinate to the inner and the outer surface. The model is subsequently converted into a rectangular Cartesian coordinate system with the long axis of the ventricle oriented along the x-axis and the y-axis directed toward the centre of the right ventricle. The resulting model consists of 16 finite elements with its geometry being interpolated in radial direction using linear Lagrange basis functions and in circumferential and longitudinal direction using cubic Hermite basis functions.

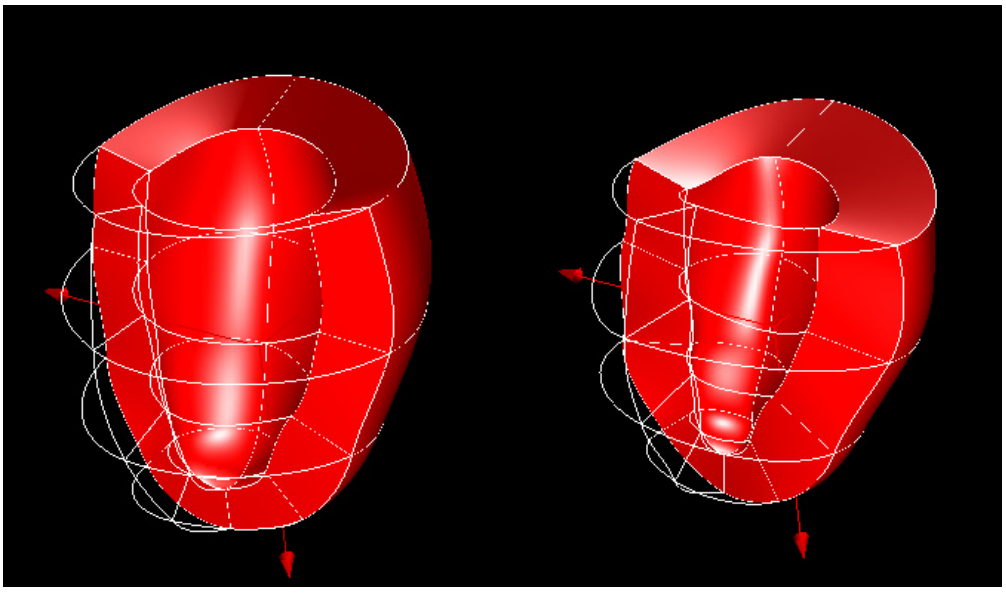

Figure 4. The finite element model of the left ventricle at end-diastole (a) and end-systole (b).

Model geometries were generated for 9 time steps equally spaced over half a heart cycle from end-diastole to end-systole. End-diastole is determined by the rising R wave of the ECG, whereas end-systole is defined as the instant of least cavity area in the midventricle [4]. Determining the correct moment of end-systole is difficult because there is a period of isovolumic relaxation in which both aortic and mitral valves are shut and the volume is constant. This period lasts 50-100 milliseconds.

Since the strain field is computed from the deformation between end-diastole and end-systole we only consider the model at these two moments. Images of the model at maximum expansion and maximum contraction are shown in figure 4.

Strain information was obtained from tagged MRI images as shown in figure 5. MR tissue tagging is a useful imaging tool for the non-invasive quantification of heart wall motion [12]. Typically, multiple parallel tagging planes of magnetic saturation are created orthogonal to the imaging plane in a short time interval ($\sim$10 msec) after detection of the R wave. The intersection of these tagging planes with the image plane gives rise to dark stripes $\sim$1 mm in width and spaced $\sim$6 mm apart. The image stripes deform with

the underlying tissue and fade according to the longitudinal relaxation time constant T1 (∼800 msec for myocardium). Techniques for image stripe tracking and reconstruction of the 3D displacement field using a finite element model have been developed and validated [24,25]. From the model, kinematic parameters such as strain can be calculated at any point.

The strain field is represented by 10x10x6 sample points per element with 10 sample points each in circumferential and longitudinal direction and 6 sample points in radial direction. No strain values are defined along the longitudinal axis where the four apical finite elements meet. This is the case because the elements have a singularity along that line (the derivative in circumferential direction is undefined) so that the strain values at these position are unreliable. In order to get a continuous visualization we generate strain tensors for these points by averaging for each points its direct neighbours in longitudinal direction. Each strain value is defined with respect to the material coordinate system, i.e., the normal components of a tensor represent the strains in circumferential, longitudinal and radial direction, respectively. The computation of the strain field was validated using a gel phantom [25].

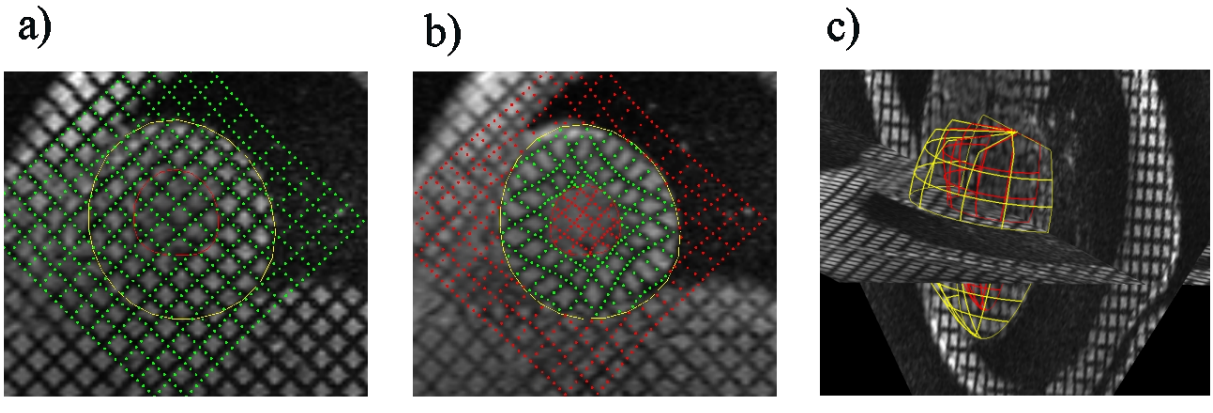

Figure 5. Tag lines before (a) and after (b) myocardial contraction and the fitted epicardial and endocardial surface (c).

In the following discussion we evaluate and visualize two models of the left ventricle. The first model, shown in figures 4 and 6, represents a healthy left ventricle. The second model, shown in figure 7, is from a heart diagnosed with non-ischemic *dilated cardiomyopathy*, which is characterized by cardiac enlargement, increased cardiac volume, reduced ejection fraction, and congestive failure [26].

4. Computing Ventricular Performance Measures

The performance of the left ventricle is often specified using various length, surface and volume measures such as its systolic and diastolic volume and its ejection fraction. Using

our visualization toolkit the user can specify elements, faces and parameter curves and compute their volume, area and length, respectively.

4.1. Computing Volume Measures

The volume of a single element is obtained by integrating the identity function over the finite element in world coordinates. The calculation is simplified by using the substitution rule of multi-dimensional integration [27, p.478]

$$\int_{\mathbf{x}(\Omega)} f(\mathbf{u})\, d\mathbf{u} = \int_{\Omega} f(\mathbf{x}(\boldsymbol{\xi}))|det\mathbf{J}(\boldsymbol{\xi})|\, d\boldsymbol{\xi} \tag{10}$$

where f is the identity function, Ω is the unit cube representing the domain of the parent element, $\mathbf{x}(\boldsymbol{\xi})$ is the transformation function from ξ-coordinates to world coordinates and $\mathbf{J}$ is its Jacobian. The resulting integral can be evaluated efficiently using Gaussian Quadrature [28]. Determining the degree of each ξ-coordinate in the polynomial expression inside the integral shows that 5 gauss points in ξ_1 and ξ_2 direction and 2 gauss points in ξ_3 direction are sufficient to achieve exact integration.

	ED	ES	Myocardial volume reduction
Healthy heart	217.5	159.1	26.85%
Sick heart	336.7	305.3	9.32%

Table 1
Myocardial volume (in cm^3) of the healthy and the sick heart at end-diastole (ED) and end-systole (ES).

Table 1 shows the volume of the heart muscle at end-diastole and end-systole and the resulting volume reduction during contraction. In general the myocardium is considered incompressible but Denney and Prince estimate that small volume changes up to 10% occur due to myocardial perfusion [29]. Our results show considerable higher values for the healthy heart. A possible explanation is that the wall thickening strain appears to underestimate the actual strain. We believe this is due to the fact that thickening increases dramatically toward the endocardium (due to the nearly incompressible nature of the muscle) and the tag resolution of one or two stripes across the wall is inadequate to capture this.

One of the most important measures of cardiac performance is the ventricular (blood) volume and the fraction of blood ejected during contraction. In order to apply the volume computation introduced above the left-ventricular cavity must be modeled by finite elements. Using our toolkit we can define centroids for any four vertices on the endocardial surface with common longitudinal ξ-coordinate. Connecting these vertices to the corresponding points on the endocardial surface results in 16 finite elements for the left ventricular cavity.

Figure 6 and 7 show the finite element models of the ventricular cavity of the healthy and sick heart at end-diastole and end-systole.

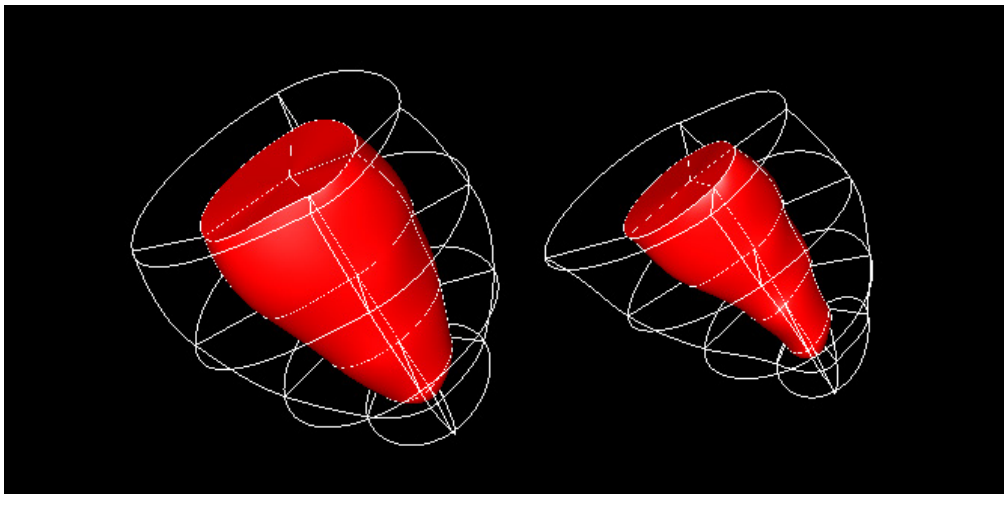

Figure 6. Ventricular cavity of the healthy heart at end-diastole (left) and end-systole (right).

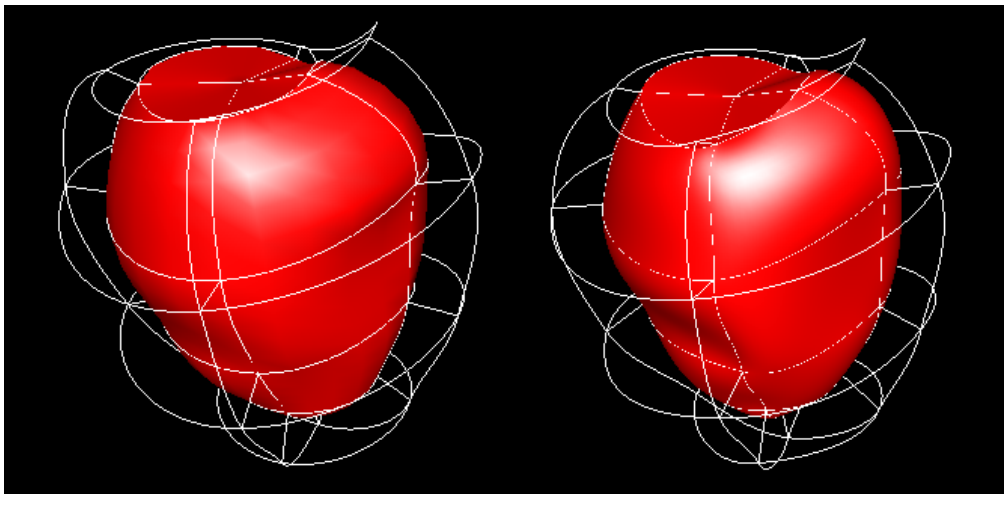

Figure 7. Ventricular cavity of the sick heart at end-diastole (left) and end-systole (right).

Using equation 10 we can now compute the left ventricular volumes at end-diastole (ED) and end-systole (ES). The difference of these values represents the stroke volume [volume of ejected blood] (SV) and the ratio of stroke volume to the volume at end-diastole represents the ejection fraction (EF). The results for the healthy and diseased heart are shown in table 2.

	ED	ES	SV	EF
Healthy heart	87.15	35.08	52.07	59.75%
Sick heart	314.18	277.94	36.23	11.53%

Table 2
Ventricular volume (in cm^3) of the healthy and diseased left ventricle at end-diastole (ED) and end-systole (ES), stroke volume (SV), and ejection fraction (EF).

The ventricular volume of the healthy heart at end-diastole is about $87cm^3$ and the stroke volume is $52cm^3$ resulting in an ejection fraction of about 60%. These values correspond well with data reported in the medical literature [30]. We think that the values slightly underestimate the actual ejection fraction due to the difficulties with computing the radial strain. The current model does not track tags at the endocardial boundary which might give a better approximation of inner wall motion.

For the diseased heart a considerable larger end-diastolic volume is observed. However, the stroke volume is only $36.23cm^3$ and about 30% smaller than for the healthy heart. The ejection fraction is only 11.5%. These values indicate a severe impairment of myocardial function.

4.2. Computing Ventricular Surface Areas

The area of a surface $\mathbf{\Phi} = \mathbf{\Phi}(u, v)$ over a parameter region K is computed by [27, p.505]

$$I(\Phi) = \int_K \left| \frac{\partial \mathbf{\Phi}}{\partial u} \times \frac{\partial \mathbf{\Phi}}{\partial v} \right| d(u,v) =$$

$$\int_K \sqrt{\left| \begin{matrix} \frac{\partial \Phi_2}{\partial u} & \frac{\partial \Phi_2}{\partial v} \\ \frac{\partial \Phi_3}{\partial u} & \frac{\partial \Phi_3}{\partial v} \end{matrix} \right|^2 + \left| \begin{matrix} \frac{\partial \Phi_3}{\partial u} & \frac{\partial \Phi_3}{\partial v} \\ \frac{\partial \Phi_1}{\partial u} & \frac{\partial \Phi_1}{\partial v} \end{matrix} \right|^2 + \left| \begin{matrix} \frac{\partial \Phi_1}{\partial u} & \frac{\partial \Phi_1}{\partial v} \\ \frac{\partial \Phi_2}{\partial u} & \frac{\partial \Phi_2}{\partial v} \end{matrix} \right|^2} d(u,v)$$

We are only interested in surfaces parallel to one of the material coordinate axes. For example, the endocardial surface is given by the coordinate planes in material space with $\xi_3 = 0$. In this case $\mathbf{\Phi}(\xi_1, \xi_2) = \mathbf{x}(\mathbf{f}(\xi_1, \xi_2))$ where $\mathbf{f}(\xi_1, \xi_2) = (\xi_1, \xi_2, 0)$ and

$$\frac{\partial \mathbf{\Phi}}{\partial \xi_1} = \frac{\partial \mathbf{x}}{\partial f_1}\frac{\partial f_1}{\partial \xi_1} + \frac{\partial \mathbf{x}}{\partial f_2}\frac{\partial f_2}{\partial \xi_1} + \frac{\partial \mathbf{x}}{\partial f_3}\frac{\partial f_3}{\partial \xi_1} = \frac{\partial \mathbf{x}}{\partial f_1} = \frac{\partial \mathbf{x}}{\partial \xi_1} \tag{11}$$

and similarly for the other partial derivatives. The surface area A is therefore given by

$$A = I(\Phi) = \int_0^1 \int_0^1 \sqrt{\left| \begin{matrix} \frac{\partial x_2}{\partial \xi_1} & \frac{\partial x_2}{\partial \xi_2} \\ \frac{\partial x_3}{\partial \xi_1} & \frac{\partial x_3}{\partial \xi_2} \end{matrix} \right|^2 + \left| \begin{matrix} \frac{\partial x_3}{\partial \xi_1} & \frac{\partial x_3}{\partial \xi_2} \\ \frac{\partial x_1}{\partial \xi_1} & \frac{\partial x_1}{\partial \xi_2} \end{matrix} \right|^2 + \left| \begin{matrix} \frac{\partial x_1}{\partial \xi_1} & \frac{\partial x_1}{\partial \xi_2} \\ \frac{\partial x_2}{\partial \xi_1} & \frac{\partial x_2}{\partial \xi_2} \end{matrix} \right|^2} d\xi_1 d\xi_2 \tag{12}$$

where the partial derivatives $\frac{\partial x_i}{\partial \xi_j}$ are the entries of the Jacobian $\mathbf{J}$ of the coordinate transformation function $\mathbf{x}(\boldsymbol{\xi})$. The integral is again evaluated by gauss integration. Simulations showed that even though the integrand is not polynomial the gauss integration gives five figure accuracy [5].

	ED	ES	Area reduction
Epicardial surface healthy heart	201.7	147.7	26.75 %
Endocardial surface healthy heart	93.4	53.4	42.76 %
Epicardial surface sick heart	350.6	324.6	7.40 %
Endocardial surface sick heart	218.7	200.0	8.55 %

Table 3
Surface area (in cm^2) of the endocardial and the epicardial surface of the healthy and sick left ventricle at end-diastole (ED) and end-systole (ES).

Table 3 shows the areas of the endocardial and the epicardial surface. It can be seen that the area reduction of the sick left ventricle is severely impaired. Since the muscle fibers of the myocardium are aligned with these surfaces the measurements indicate that either muscle fiber don't contract (e.g., due to fibrosis) or that they contract in some regions but expand in other regions of the surface. In order to further examine this deformation behaviour we will visualize the strain tensor in section 6.

Using the above technique it is also possible to compute the midventricular cavity cross-sectional area. We get as results $13.27cm^2$ at end-diastole and $5.81cm^2$ at end-systole. From these values we determine a mid ventricular radius of $2.06cm$ at end-diastole and $1.36cm$ at end-systole.

4.3. Computing Length Measures

Similar to the volume and area computations it is also possible to compute the arc-length of a parametric function $\gamma : [a, b] \rightarrow \mathbb{R}^3$ [27, p.354]

$$L(\boldsymbol{\gamma}) = \int_a^b |\dot{\boldsymbol{\gamma}}(t)|dt = \int_a^b \sqrt{\dot{\gamma_1}^2 + \dot{\gamma_2}^2 + \dot{\gamma_3}^2}dt \tag{13}$$

Assume the start point and end point of a parameter curve within a finite element are ξ_s and ξ_e. Then the curve in material coordinates is the linear line segment $\boldsymbol{\gamma}(t) = \boldsymbol{\xi}^s + t(\boldsymbol{\xi}^e - \boldsymbol{\xi}^s)$ with $t \in [0, 1] = [a, b]$ so that

$$\dot{\boldsymbol{\gamma}}(t) = \mathbf{J}(\boldsymbol{\gamma})(\boldsymbol{\xi}^e - \boldsymbol{\xi}^s) \tag{14}$$

where $\mathbf{J}$ is again the Jacobian of the transformation function from ξ-coordinates to world coordinates.

Using this measure it is possible to compute the length of a circumflex arc of a ventricle by the length of a curve on the endocardial surface with a constant longitudinal ξ-parameter. The length of this curve can then be used to derive a value for the ventricular radius at that position. However, reliable results are only obtained if the arc is

approximately planar and orthogonal to the long axis of the ventricle. While the technique could also be used to approximate the wall thickness at a point it does not necessarily yield the shortest distant between the endocardial and epicardial surface. Better computational techniques are suggested in [31].

5. A Visualization Toolkit

The next section examines the deformation of the heart by using 3D visualizations. All visualizations are created using a toolkit we designed for biomedical datasets and models [5]. The toolkit, a screenshot of which is shown in figure 8, was programmed in C/C++ and uses OpenGL, GLU, GLUT and FLTK, a LGPL'd C++ graphical user interface toolkit for X (UNIX), OpenGL, and WIN32 [32].

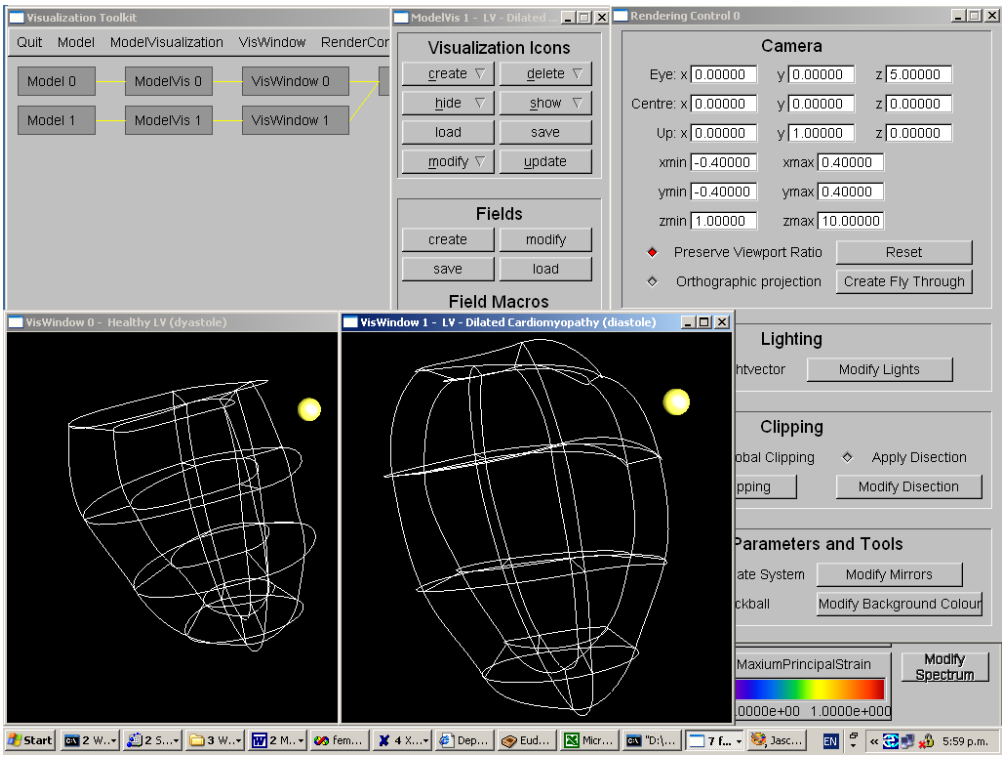

Figure 8. A screen shot of the visualization toolkit. The yellow spheres indicate the septal wall of the left ventricle.

Three features of our toolkit are worth mentioning. The first feature is a modular object-oriented (OO) design with separate objects describing input data sets, visualization icons, rendering parameters, and visualization windows. A visualization is achieved by defining relationships, subject to some constraints, between these objects. The design facilitates the definition of simultaneous visualizations of multiple models such as the

simultaneous display of a sick and a healthy heart as shown in figure 8. Using the same rendering parameters ensures that both models are displayed using the same view, scaling, orientation and lighting. Similarly the same model can be displayed in multiple windows making it possible, for example, to use simultaneously a global and a local view.

The second feature is a generalised field data structure that allows the user to mix data sets from different sources such as finite element data, MR or PET raw data and analytical data in the form of algebraic functions [33]. Finite element data can be represented in material and world coordinates and new fields can be interactively derived using a simple to use graphical user interface. Figure 9 shows the graphical user interfaces for constructing new fields (left) and for defining macros for commonly used derived fields (right).

The advantages of our field data structure are threefold:

- We eliminate problems with the interpolation of derived values. For example, directly interpolating the eigenvalues of a tensor over a finite element gives usually the wrong results. Instead we rather interpolate the tensor and compute the eigenvalues from the resulting tensor.

- We can combine arbitrary fields through arithmetic functions (e.g., the difference between two scalar fields) even if they are defined over different grids. Similarly, we can interactively derive new fields by choosing a parent field for a derived fields.

- No additional sample errors are introduced as would happen, for example, when sampling an analytic field in order to create a new field over a given fixed grid structure.

- Entities defined over a finite element grid can be represented with respect of either the world coordinates or the material coordinates. This choice of representation increases the power of the visualization [5].

Finally our toolkit contains a variety of visualization techniques which can be applied to the data set using various element and point selection tools. A global colour map control makes it possible that icons for different visualizations use the same colour maps which facilitates the comparison of multiple models. Defining new colour maps is often necessary to avoid colour clashes when displaying various visualization icons simultaneously and gives the user additional freedom when exploring the data set. A colour map can be modified to be exponential (colour spectrum is reparameterized with an exponential function) or cyclical (colour map consists of multiple cycles of the colour spectrum). An exponential colour map improves the perception of qualitative information when using predominantly evenly distributed fields with small extremal regions. Cyclical colour maps have the advantage of giving gradient information without inducing visual cluttering. They are therefore useful when examining symmetry patterns and discontinuities in a scalar field [34].

6. The Visualization of Myocardial Strain

The measurements presented in section 4 indicated a severe impairment of the contraction of the sick heart. In order to better understand the local deformation of the

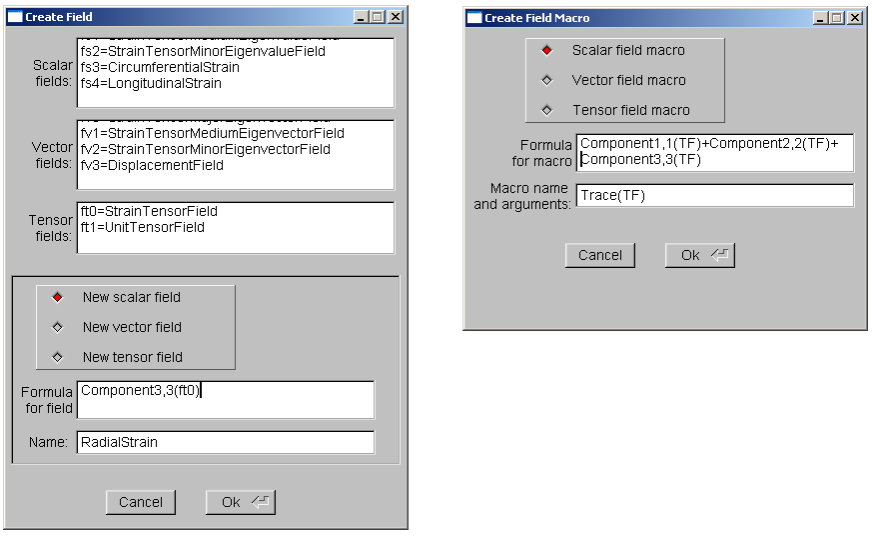

Figure 9. Graphical user interfaces for creating new fields from arithmetic expressions (left) and for creating macros (right).

myocardium more information is required. This section presents and explains various visualizations of the strain tensor and of quantities derived from it. Most visualization methods in this section visualize the strain tensor by using its principal directions and principal strains explained in subsection 1.2.

6.1. Tensor Ellipsoids

As an initial visualization we display tensor ellipsoids at regular sample point throughout the midmyocardium. Tensor ellipsoids encode the principal directions and strains by the directions and lengths, respectively, of the axes of the ellipsoid. In order to encode the sign of an eigenvalue we divide an ellipsoid into six segments using a hexagonal subdivision of the unit sphere. A red segment indicates expansion and a blue segment indicates contraction. Note that the 3D geometry is difficult to perceive from a static image. Rotating the model enables the brain to differentiate ellipsoids in the foreground and background. Consequently our toolkit incorporates a function to animate the trackball which is used to rotate the model.

Figure 10 shows that for the healthy ventricle the myocardium expands in the radial direction (wall thickening) and contracts in the longitudinal and circumferential direction with the circumferential contraction being in general larger. The contraction is smallest in the septum and largest in the free wall. The results correspond well with measurements reported in the literature [35,11,4,36].

The deformation of the sick ventricle is highly abnormal. Whereas the anterior-lateral wall of the ventricle displays an almost normal deformation behaviour, albeit with smaller strain values, the situation is the exact opposite in the septal wall of the ventricle. Here the myocardium is contracting in the radial direction and is expanding in the circumferential and longitudinal direction.

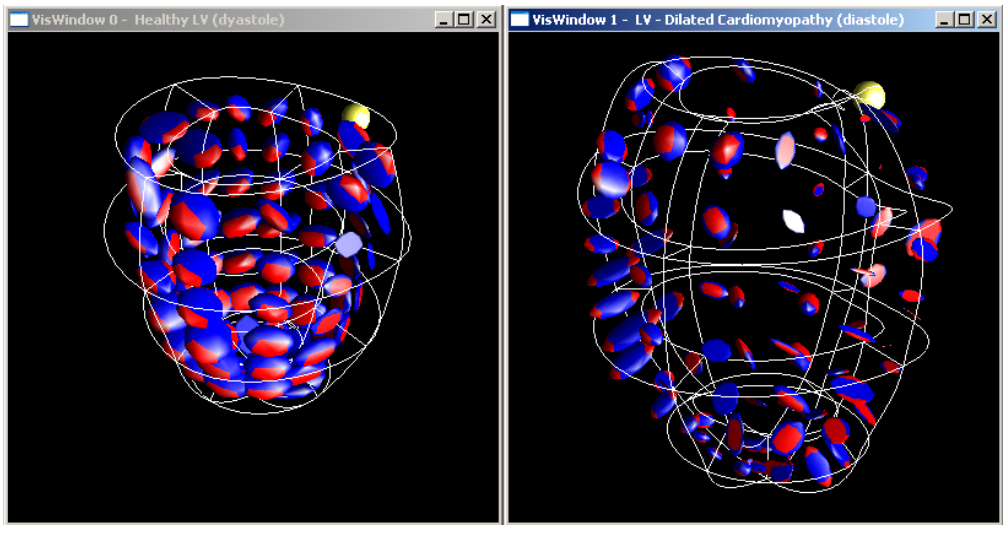

Figure 10. The strain field in the midwall of the healthy (left) and diseased (right) left ventricle visualized using tensor ellipsoids. The septal wall is indicated by a yellow sphere.

6.2. Streamlines

While tensor ellipsoids contain the complete tensor information the resulting visualization suffers from visual cluttering. Furthermore information is only displayed at selected sample points. A continuous representation of a vector field (e.g., an eigenvector field) along a line is obtained by using *streamlines* which are at each point tangential to the underlying vector field. Mathematically a streamline can be described as an integral curve $\mathbf{x}(s)$ which satisfies

$$\frac{d\mathbf{x}}{ds} = \mathbf{v}(\mathbf{x}(s)) \ , \qquad \mathbf{x}(0) = \mathbf{x}_0 \tag{15}$$

where $\mathbf{v}(\mathbf{x})$ is a vector field and the initial condition $\mathbf{x}(0)$ defines the starting point $\mathbf{x}_0$ of the streamline.

In general the above system of equations has no analytic solution and is solved by numerical integration. Standard techniques for streamline integration include fixed step size integrators such as the Euler, Midpoint or Runge-Kutta method. A faster computation can be achieved by adaptive step size integration [37,38]. If the step size is too large or the curvature is too high a dense sampling of the streamline might be required in order to obtain a good visual approximation of it. The sampling can be performed as a post-integration interpolation step [39] or by using a specialised integrator which produces an interpolation from the integration information [38, pp.176].

Figure 11 uses colour mapped streamlines to visualize the direction and magnitude of the major principle strain. Note that an eigenvector field is unsigned (i.e., eigenvectors have a direction but not an orientation) and that therefore streamlines must be integrated in both the positive and the negative direction of the eigenvector field.

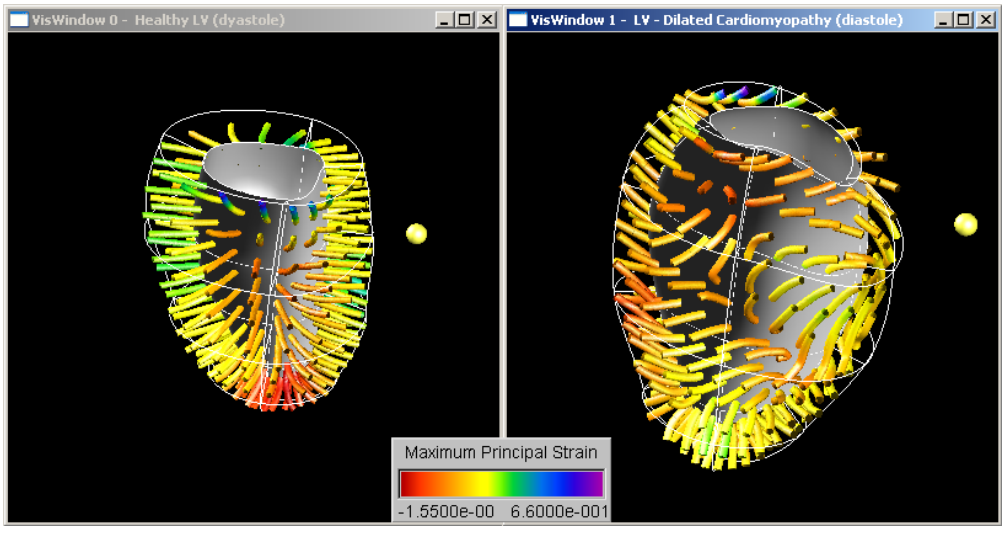

Figure 11. The strain field in the midwall of the healthy (left) and the diseased (right) left ventricle visualized using streamlines in the direction of the major principal strain. The septal wall is indicated by a yellow sphere.

Streamlines are rendered as thin tubes with a constant diameter rather than as lines. Illuminating these tube-like structures gives important shape and depth cues which aid their 3D perception [40]. We also render the endocardial wall (in gray) in order to reduce visual cluttering caused by the overlap of streamlines in the foreground and the background.

The image on the left of figure 11 shows clearly that for the healthy heart the major principal strain is oriented in radial direction throughout the myocardial wall and that it is positive and increases toward the endocardium. This observation is consistent with an increased wall thickening towards the endocardium.

The image on the right of figure 11 confirms the previously identified abnormal contraction of the diseased left ventricle. The direction of the major principal strain is normal in the anterior-lateral and the inferior-lateral wall. However, the magnitude of the major principal strain in the inferior-lateral wall is considerably smaller than for the healthy heart and is negative in some regions (indicating a wall thinning instead of a wall thickening). In the septal wall of the diseased heart the maximum principal strain is oriented in longitudinal and circumferential direction rather than in radial direction.

6.3. Hyperstreamlines

Streamlines encode only one eigenvector. A continuous representation of the complete strain tensor along a line is achieved by using hyperstreamlines [41].

The trajectory of a hyperstreamline is a streamline in an eigenvector field as described in the previous subsection. The other two eigenvectors and corresponding eigenvalues of the strain tensor define the axes and lengths of the ellipsoidal cross section of the hyperstreamline. The remaining eigenvalue is colour mapped onto the hyperstreamline.

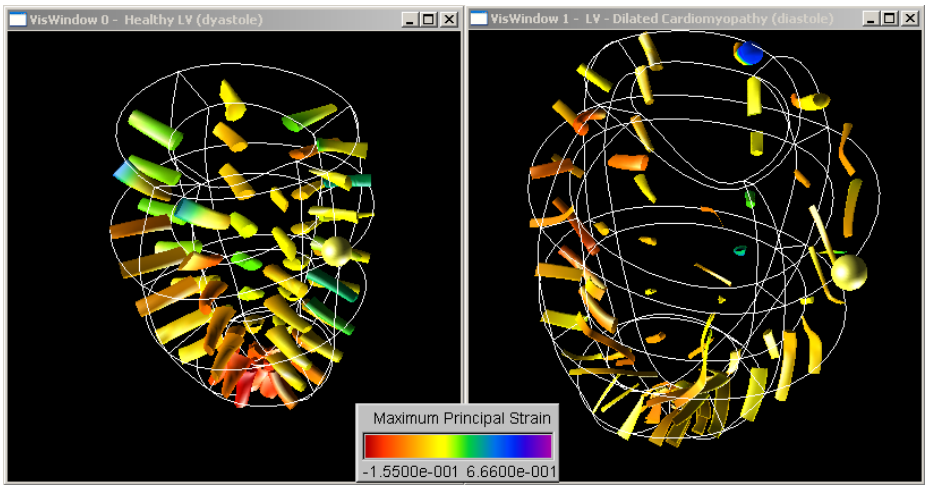

Figure 12. The strain field in the midwall of the healthy (left) and the diseased (right) left ventricle visualized using hyperstreamlines in the direction of the major principal strain. The septal wall is indicated by a yellow sphere.

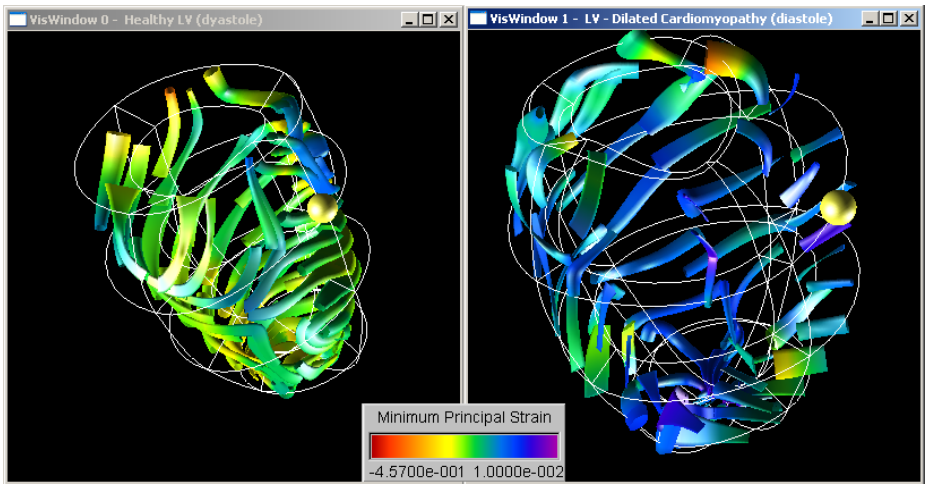

Figure 13. The strain field in the midwall of the healthy (left) and the diseased (right) left ventricle visualized using hyperstreamlines in the direction of the minor principal strain. The septal wall is indicated by a yellow sphere.

Figure 12 and 13 show hyperstreamlines in the direction of the major and minor principal strain, respectively.

The image on the left of figure 12 shows again that for the healthy heart the major principal strain is oriented in radial direction throughout the myocardial wall and that it is positive and increases toward the endocardium. Furthermore it can be seen from the diameter of the cross section of the hyperstreamline that with the exception of the septal wall the magnitude of the transverse strains increases from the epicardial to the endocardial surface. We are not aware of any previous work showing all these properties with a single image.

The minimum principal strain of the healthy left ventricle is compressive throughout most of the myocardium and its direction resembles over most of the myocardium a spiral moving toward the apex. This strain direction corresponds well with the motion of the heart described in the medical literature: The septum performs initially an anticlockwise rotation (apex-base view) but later a more radial movement. The apex rotates overall anticlockwise whereas the base rotates clockwise. The anterioseptal regions of the mid and apical levels and the posterioseptal region of the base perform a hook-like motion because of a reversal of rotation [4]. Note that we have in the inferior-septal region an interesting feature where the hyperstreamlines change suddenly their direction.

6.4. Line Integral Convolution

The above described feature where hyperstreamlines change direction can be examined in more detail using a line integral convolution texture.

Line Integral Convolution (LIC) is an effective method to visualize vector fields by using curvilinear filters to locally blur an input noise texture I along a vector field $\mathbf{v}$. The steps of the algorithm, as originally proposed by Cabral and Leedom [42], are indicated in figure 14.

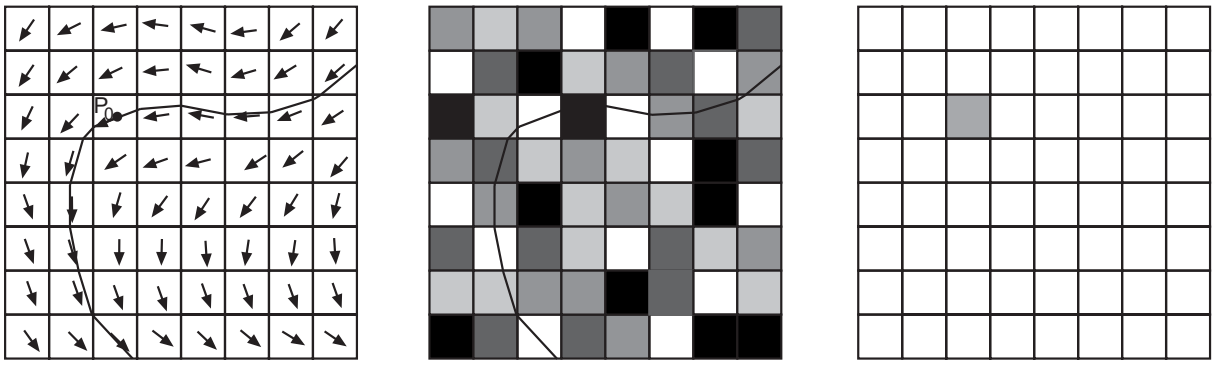

Figure 14. Vector field with a streamline through the pixel with the centre p_0 (left), white noise input texture (middle), and the output texture of the pixel (right).

For any pixel $I(q, r)$ of the input texture the centre $\mathbf{p}_0$ of it is used as the centre of a

streamline which is advected forwards and backwards by a length L. The pixels covered by the streamline are hence in forward direction

$$\mathbf{p}_i = \mathbf{p}_{i-1} + \frac{\mathbf{v}(\mathbf{p}_{i-1})}{\|\mathbf{v}(\mathbf{p}_{i-1})\|}\Delta s_{i-1} \tag{16}$$

where Δs_{i-1} is the distance to the pixel boundary and $s_{i+1} = s_i + \Delta s_i$. Pixels covered in backward direction are defined similarly and are indicated by negative indices. For each line segment $[s_i, s_{i+1}]$ of the streamline covering pixel p_i an exact integral of the convolution kernel $k(w)$ is computed and used as weight in the LIC

$$h_i = \int_{s_i}^{s_i+\Delta s_i} k(w)dw \tag{17}$$

The output pixel $O(q, r)$ is then given by

$$O(q,r) = \frac{\sum_{i=-l}^{l} I(\mathbf{p}_i)h_i}{\sum_{i=-l}^{l} h_i} \tag{18}$$

where l is chosen such that the $\sum_{i=-l}^{l} s_i = 2L$. Vector magnitude is represented either by using colour mapping or by varying the length L of the filter kernel.

Parameters influencing the quality of the output texture are the input texture, the filter kernel, and the length of the convolution length. Most authors employ an input texture based on white noise which has a constant power spectrum and is completely random. Aliasing effects due to high frequency components in the white noise texture can be reduced by low-pass filtering the input texture [42].

We use the direction of the minor principal strain as a vector field and use its magnitude to colour map the texture. Additional details are found in [5].

Figure 15 shows that the maximum compressive strain in the midmyocardium is predominantly oriented in circumferential direction with a slight downward tilt. Several interesting points exist where the strain suddenly changes direction. Results from tensor analysis show that these points are *degenerate points* for which at least two eigenvalue are equal [43]. An example of such a point is indicated by the white rectangle and is shown enlarged on the right hand side of the image. We found that most of the degenerate points occur on or near the septal wall. The unusual variations in strain orientation might be caused by the right ventricular wall which is connected to the left ventricular wall at both sides of the septum. In contrast the strain field of the sick heart contains considerable more degenerate points distributed throughout the myocardium.

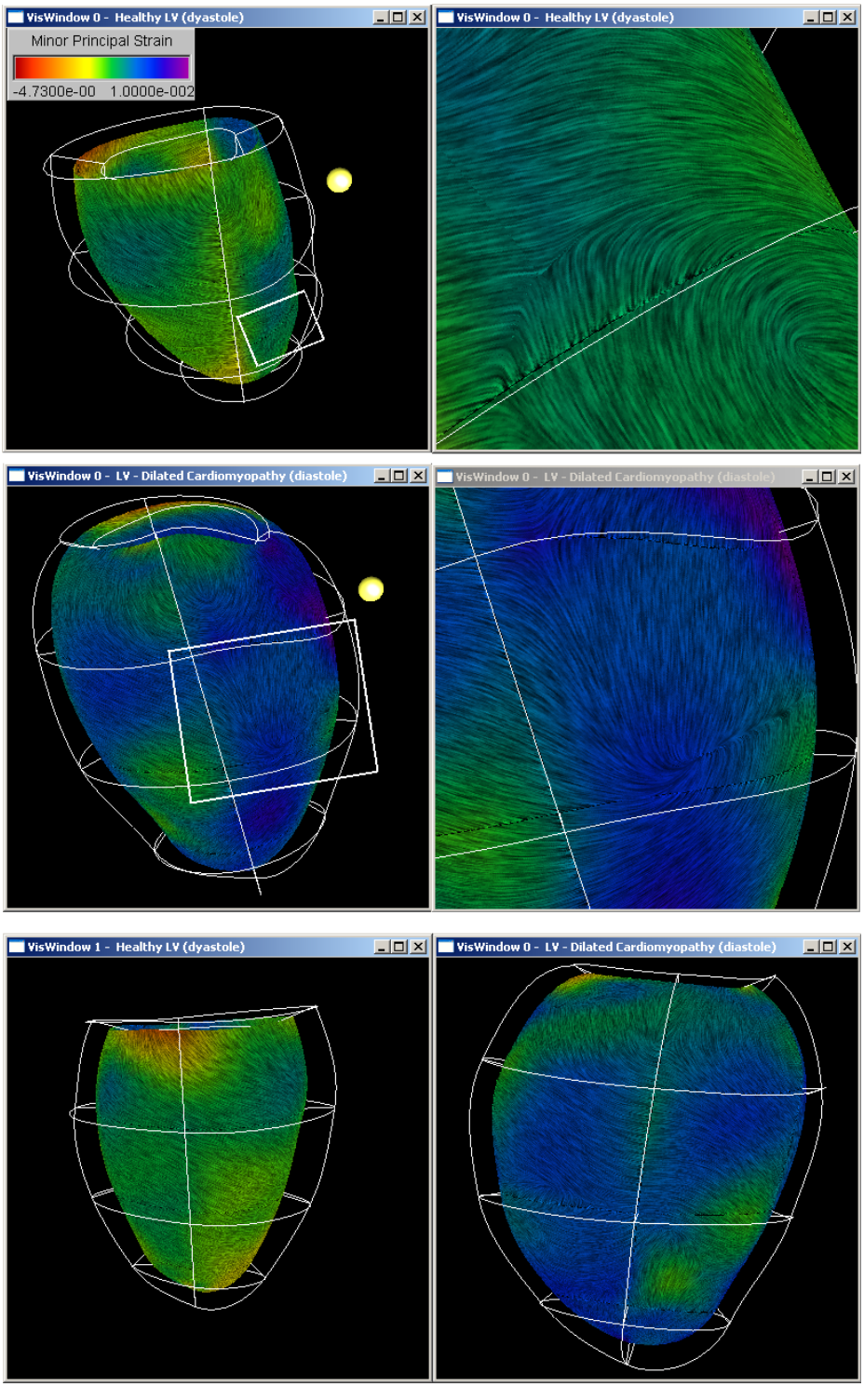

Figure 15. The minor principal strain (maximum contracting strain) of the healthy (top) and sick (middle) heart visualized using Line Integral Convolution. The bottom images show the lateral wall of the healthy (left) and sick (right) heart.

6.5. Colour Mapped Surfaces and Isosurfaces

We conclude this section with an examination of the distribution of the strains in the material directions. Since the strain tensor is defined with respect to the material coordinates the strains in circumferential, longitudinal and radial direction are given by the normal components E_{11}, E_{22} and E_{33}, respectively, of the strain tensor $\mathbf{E}$.

Figure 16 visualizes the normal strains on the endocardial surface using colour mapping and shows additionally the 0-isosurface, which separates contracting and expanding regions. The isosurface was computed with a modified *Marching Cubes* algorithm in material space [5].

The images on the left of the figures show clearly that the healthy left ventricle contracts in circumferential and longitudinal direction and expands in radial direction. The only exceptions are some parts of the model boundary and, for the radial strain, three small cylindrical regions at the apex and the septal and lateral wall. All three normal strain components are distributed relatively evenly over the endocardial surface.

For the diseased heart the lateral wall and part of the anterior and inferior wall contract in circumferential and longitudinal direction. Wall thickening is observed in the basal-lateral wall, the basal-septal wall and in parts of the anterior and inferior wall. The rest of the myocardium shows an abnormal deformation. As a result of the strain distribution the ventricle does not contract evenly but rather performs a shape change.

We are also interested in the shear components of the strain tensor. It is known that during contraction the heart changes predominantly in diameter. LeGrice et al. [44] reports 8% lateral expansion but 40% wall thickening. This indicates reorganization of the myocytes during systole. Because of the sheet structure of the myocardium it has been proposed that the sheets can slide over another restricted mainly by the length of the interconnecting collagen fibers [44]. The shear properties of the myocardium resulting from this sliding motion are characterized in [45,46]. The shear is most restricted in the direction of the sheet normals and the maximum shear is possible in the fiber direction. Wall shear is thought to be an important mechanism of wall thickening during systole and therefore may play a substantial role in the ejection of blood from the ventricle.

Figure 17 shows the shear in the circumferential-longitudinal plane. For the healthy heart the shear strain is positive for most of the myocardium with the exception of some subepicardial regions close to the merging point with the right ventricular wall. No consistent behaviour can be found for the diseased heart. The shear in the lateral wall resembles most closely the normal range of values whereas the anterior-basal region exhibits extremely high negative strains, which might indicate impending tissue damage.

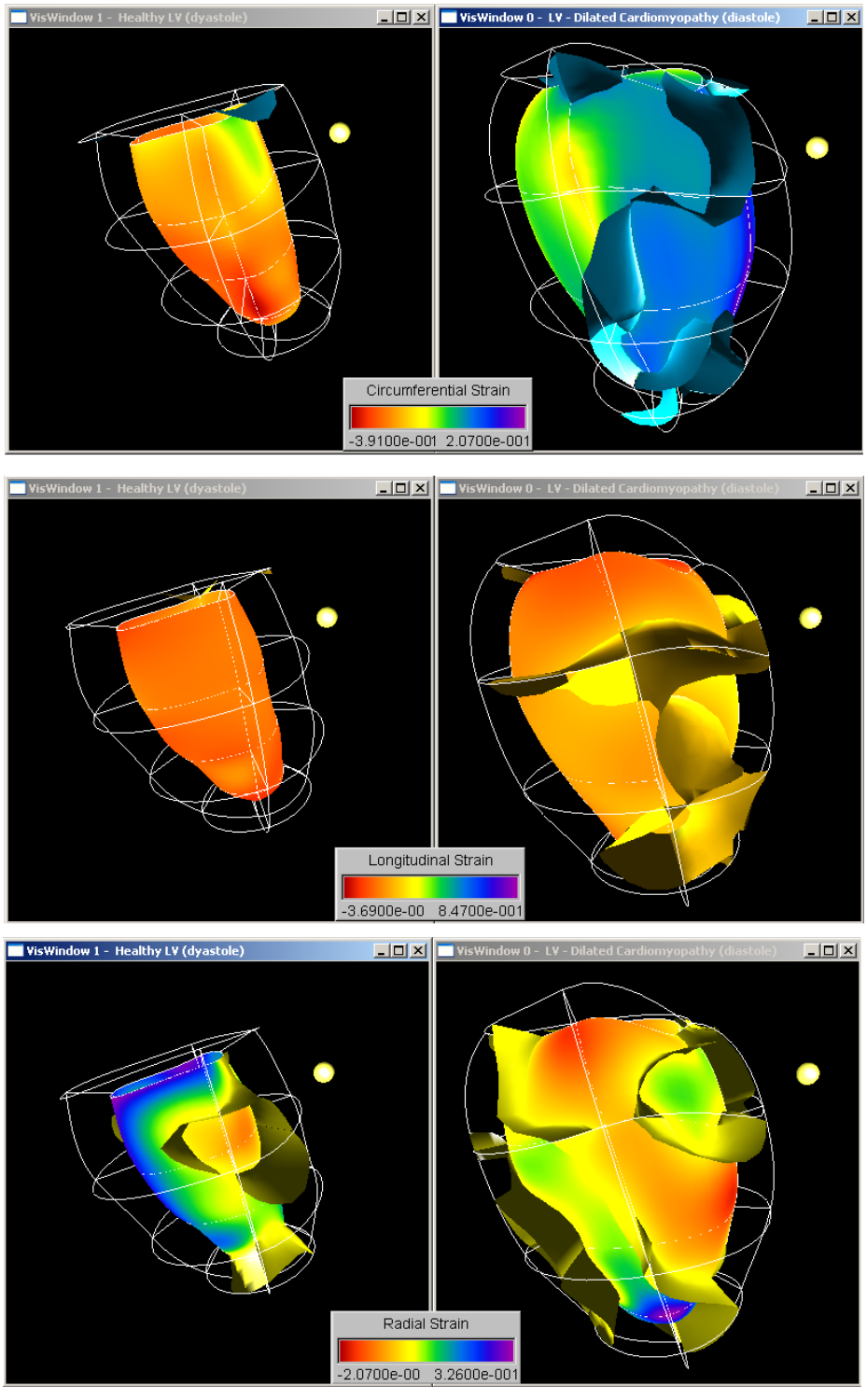

Figure 16. The normal strain in circumferential (top), longitudinal (middle) and radial (bottom) direction on the endocardial surface of the healthy (left) and sick (right) heart. The images show also the 0-isosurface which separates region of contractile and expanding strain. The septal wall is indicated by a yellow sphere.

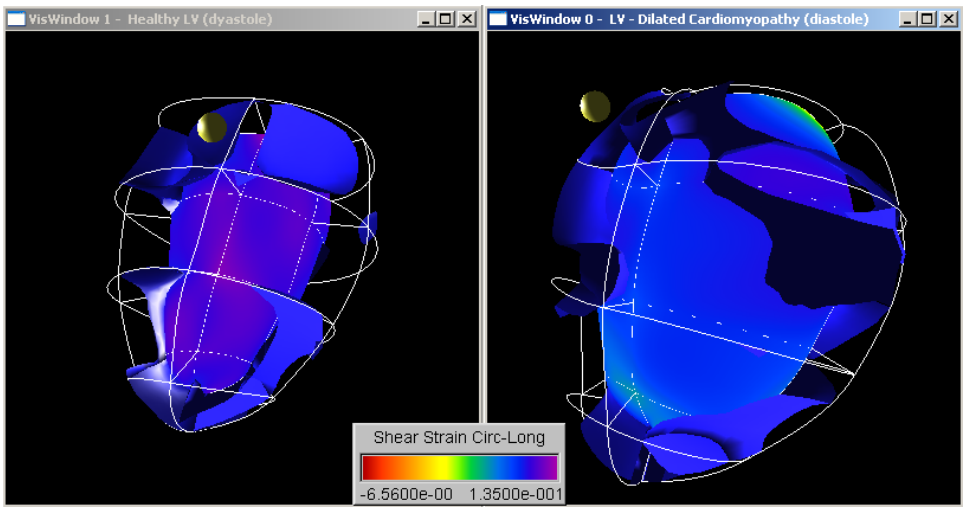

Figure 17. The circumferential-longitudinal shear strain component in the healthy (left) and sick (right) heart visualized using a colour map and the 0-isosurface. The septal wall is indicated by a yellow sphere.

7. Conclusion

Visualizing the strain field improves the understanding of the complex deformation of the heart muscle. Using techniques new to the biomedical field offers additional insight. The visual information can be supplemented by computing ventricular performance measures which are easily obtained from the finite element model using numerical integration.

The visualization of the healthy heart confirms observations previously reported in the literature. Using tensor ellipsoids, streamlines and hyperstreamlines makes it possible to visualize complex deformation behaviour in a single image. Line integral convolution uncovers the presence of degenerate points at which the principal strains suddenly change direction. Further investigations are necessary to find the relationship between degenerate points, fiber structure, and the ventricular anatomy. Furthermore we want to explore their significance (if any) for diagnosing heart diseases.

Visualizing a ventricle with dilated cardiomyopathy showed that the deformation of the lateral wall resembles most closely the expected motion whereas the septal wall behaved almost contrary to the expected deformation. Very large negative shear strains were recorded in the anterior-basal wall of the ventricle. The combined effect of these deformations seems to be a pumping action by shape deformation (from circular to ellipsoidal cross section) rather then by contraction.

The visualizations and measurement performed in this paper demonstrated the usefulness of our visualization toolkit for exploring biomedical models. Using the unique field data structure enables the interactive definition of new measures and facilitates the exploration of the data set. The modular OO-design allows comparison of multiple models, which is further enhanced by the user interface for colour map design and control. The toolkit provides many standard visualization techniques in use today with some improvements being implemented by us.

8. Future Research

We are interested in visualizing other data sets of diseased hearts, in particularly models of ischemic myocardium. It is known that small changes in the deformation behaviour of the myocardium occur before first symptoms of a cardiac infarct develop and we hope that visualizing myocardial strain supports the detection of regions of low blood perfusion. Non-traditional visualization methods such as hyperstreamlines, LIC and tensor topology [43,47] seem to be particularly promising for this purpose.

Of particular interest is the relationship between myocardial strain and fiber structure. Recent research suggests that measurement of the fiber structure is possible using diffusion tensor imaging [48–50]. Further information could be provided by fusing our data with functional data obtained by PET and SPECT [51].

9. Acknowledgments

We would like to thank Dr. Richard White of the Cleveland Clinic, Cleveland, Ohio, USA, who kindly provided the tagged MRI data of a left ventricle diagnosed with dilated cardiomyopathy.

REFERENCES

1. S. Masood, G.-Z. Yang, D. J. Pennell, D. N. Firmin, Investigating intrinsic myocardial mechanics - the role of MR tagging, velocity phase mapping and diffusion imaging, Journal of Magnetic Resonance Imaging 12 (6) (2000) 873–883.
2. R. W. Alexander, R. C. Schlant, V. Fuster, R. A. O'Rourke, R. Roberts, E. H. Sonnenblick (Eds.), Hurst's The Heart, 9th Edition, McGraw-Hill Companies, Inc., London, 1994.
3. A. A. Young, C. M. Kramer, V. A. Ferrari, L. Axel, N. Reichek, Three-dimensional left ventricular deformation in hypertrophic cardiomyopathy, Circulation 90 (2) (1994) 854 – 867.
4. A. A. Young, H. Imai, C.-N. Chang, L. Axel, Two-dimensional left ventricular deformation during systole using magnetic resonance imaging with spatial modulation of magnetization, Circulation 89 (2) (1994) 740 – 752.
5. B. C. Wünsche, The visualization of tensor fields in biological tissue, Ph.D. thesis, University of Auckland, (To be published) (2003).
6. B. C. Wünsche, A toolkit for visualizing biomedical data sets, in: Proceedings of GRAPHITE 2003, ANZGRAPH and SEAGRAPH, 2003, pp. 167–174.
7. G. Geskin, C. M. Kramer, W. J. Rogers, T. M. Theobald, D. Pakstis, Y.-L. Hu, N. Reichek, Quantitative assessment of myocardial viability after infarction by dobutamine magnetic resonance tagging, Circulation 98 (3) (1998) 217 – 223.
8. M. D. Cerqueira, N. J. Weissman, V. Dilsizian, A. K. Jacobs, S. Kaul, W. K. Laskey, D. J. Pernell, J. A. Rumberger, T. Ryan, M. S. Verani, Standardized myocardial segmentation and nomenclature for tomographic imaging of the heart: A statement for healthcare professionals from the cardiac imaging committee of the council of clinical cardiology of the american heart association, Circulation 105 (4) (2002) 539–542.
9. W. M. Lai, D. Rubin, E. Krempl, Introduction to Continuum Mechanics, Vol. 17 of Pergamon Unified Engineering Series, Pergamon Press, 1986.
10. T.-H. Lim, S. I. Choi, MRI of myocardial infarction, Journal of Magnetic Resonance Imaging 10 (5) (1999) 686 – 693, special Issue: Cardiovascular MRI.
11. M. A. Guttman, E. A. Zerhouni, E. R. McVeigh, Analysis of cardiac function from MR images, IEEE Computer Graphics and Applications 7 (2) (1997) 30 – 38.
12. N. Reichek, MRI myocardial tagging, Journal of Magnetic Resonance Imaging 10 (5) (1999) 609 – 616, special Issue: Cardiovascular MRI.
13. J. H. Myers, M. C. Stirling, M. Choy, A. J. Buda, K. P. Gallagher, Direct measurement of inner and outer wall thickening dynamics with epicardial echocardiography, Circulation 74 (1) (1986) 164 – 172.
14. M. D. Cheitlin, J. S. Alpert, W. F. Armstrong, G. P. Aurigemma, G. A. Beller, F. Z. Bierman, T. W. Davidson, J. L. Davis, P. S. Douglas, L. D. Gillam, R. P. Lewis, A. S. Pearlman, J. T. Philbrick, P. M. Shah, R. G. Williams, ACC/AHA guidelines for the clinical application of echocardiography: a report of the american college of cardiology/american heart association task force on practice guidelines (committee on clinical application of echocardiography), Journal of the American College of Cardiology 29 (4) (1997) 862 – 879.

15. E. Antman, J.-P. Bassand, W. Klein, M. Ohman, J. L. L. Sendon, L. Rydén, M. Simoons, M. Tendera, Myocardial infarction redefined – a consensus document of the joint european society of cardiology/american college of cardiology committee for the redefinition of myocardial infarction, Journal of the American College of Cardiology 36 (3) (2000) 959–969.
16. I. Buvat, M. L. Bartlett, A. N. Kitsiou, V. Dilsizian, S. L. Bacharach, A "hybrid" method for measuring myocardial wall thickening from gated PET/SPECT images, The Journal of Nuclear Medicine 38 (2) (1997) 324–329.
17. E. R. Holman, V. G. M. Buller, A. de Roos, R. J. van der Geest, L. H. B. Baur, A. van der Laarse, A. V. G. Bruschke, J. H. C. Reiber, E. E. van der Wall, Detection and quantification of dysfunctional myocardium by magnetic resonance imaging: A new three-dimensional method for quantitative wall-thickening analysis, Circulation 95 (4) (1997) 924–931.
18. R. Willenheimer, C. Cline, L. Erhardt, B. Israelsson, Left ventricular atrioventricular plane displacement: an echocardiographic technique for rapid assessment of prognosis in heart failure, Heart 78 (3) (1997) 230–236.
19. G. de Simone, R. B. Devereux, M. J. Koren, G. A. Mensah, P. N. Casale, J. H. Laragh, Midwall left ventricular mechanics: an independent predictor of cardiovascular risk in arterial hypertension, Circulation 93 (2) (1996) 259 – 265.
20. A. E. Schussheim, R. B. Devereux, G. de Simone, J. S. Borer, E. M. Herrold, J. H. Laragh, Usefulness of subnormal midwall fractional shortening in predicting left ventricular exercise dysfunction in asymptomatic patients with systemic hypertension, The American Journal of Cardiology 79 (8) (1997) 1065 – 1074.
21. I. Mirsky, W. W. Parmley, Assessment of passive elastic stiffness for isolated heart muscle and the intact heart, Circulation Research 33 (2) (1973) 233–243.
22. A. D. McCulloch, R. Mazhari, Regional ventricular mechanics: Integrative computational models of myocardial flow-function relations, Journal of Nuclear Cardiology 8 (4) (2001) 506–519.
23. A. Heimdal, A. Stylen, H. Torp, T. Skjrpe, Real-time strain rate imaging of the left ventricle by ultrasound, Journal of the American Society of Echocardiography 11 (1998) 1013 – 1019.
24. A. A. Young, L. Axel, Three-dimensional motion and deformation of the heart wall: Estimation with spatial modulation of magnetization - a model-based approach, Radiology 185 (1992) 241–247.
25. A. A. Young, D. L. Kraitchman, L. Dougherty, L. Axel, Tracking and finite element analysis of stripe deformation in magnetic resonance tagging, IEEE Transactions on Medical Imaging 14 (3) (1995) 413 – 421.
26. A. A. Young, S. Dokos, K. A. Powell, B. Sturm, A. D. McCulloch, R. C. Starling, P. M. McCarthy, R. D. White, Regional heterogeneity of function in nonischemic dilated cardiomyopathy, Cardiovascular Research 49 (2) (2000) 308–318.
27. H. Heuser, Lehrbuch der Analysis, Vol. 2, B.G. Teubner, 1981.
28. D. S. Burnett, Finite Element Analysis - From Concepts to Applications, Addison-Wesley Publication Company Inc., 1987.
29. T. S. Denney, Jr., J. L. Prince, Reconstruction of 3-D left ventricular motion from planar tagged cardiac MR images: An estimation theoretic approach, IEEE Transactions

on Medical Imaging 14 (4) (1995) 625 – 635.
30. L. M. Boxt, From the RSNA refresher courses: Cardiac MR imaging: A guide for the beginner, Radiographics 19 (4) (1999) 1009 – 1025.
31. R. J. van der Geest, J. H. C. Reiber, Quantification in cardiac MRI, Journal of Magnetic Resonance Imaging 10 (5) (1999) 602 – 608, special Issue: Cardiovascular MRI.
32. B. Spitzak, The FLTK home page, URL: http://www.fltk.org.
33. B. C. Wünsche, A field data structure for improved interactive exploration of scientific data sets, in: Proceedings of IVCNZ '02, 2002, pp. 13–18.
34. B. C. Wünsche, R. Lobb, The visualization of diffusion tensor fields in the brain, in: Proceedings of METMBS'01, CSREA Press, 2001, pp. 498 – 504.
35. C. H. Lugo-Olivieri, C. C. Moore, E. G.-C. Poon, J. A. C. Lima, E. R. McVeigh, E. A. Zerhouni, Temporal evolution of three dimensional deformation in the ischemic human left ventricle: Assessment by MR tagging, in: Proceedings of the 2nd Annual Meeting of the Society of Magnetic Resonance, Society of Magnetic Resonance Imaging (SMR), 1994, p. 1482.
36. T. S. Denney, Jr., E. R. McVeigh, Model-free reconstruction of three-dimensional myocardial strain from planar tagged MR images, Journal of Magnetic Resonance Imaging 7 (5) (1997) 799 – 810.
37. W. H. Press, W. T. Vetterling, S. A. Teukolsky, B. P. Flannery, Numerical Recipes in C - The Art of Scientific Computing, 2nd Edition, Cambridge University Press, 1992.
38. E. Hairer, G. Wanner, S. P. Nørsett, Solving Ordinary Differential Equations I - Nonstiff Problems, Springer Series in Computational Mathematics 8, Springer Verlag, 1993.
39. D. Stalling, H.-C. Hege, Fast and resolution independent line integral convolution, in: Proceedings of SIGGRAPH '95, 1995, pp. 249 – 256.
40. B. C. Wünsche, R. Lobb, A scientific visualization schema incorporating perceptual concepts, in: Proceedings of IVCNZ'01, 2001, pp. 31 –36.
41. T. Delmarcelle, L. Hesselink, Visualizing second-order tensor fields with hyperstreamlines, IEEE Computer Graphics and Applications 13 (4) (1993) 25 – 33.
42. B. Cabral, L. C. Leedom, Imaging vector fields using line integral convolution, in: J. T. Kajiya (Ed.), Proceedings of SIGGRAPH '93, Vol. 27, ACM SIGGRAPH, Addison Wesley, 1993, pp. 263–272.
43. T. Delmarcelle, L. Hesselink, The topology of symmetric, second-order tensor fields, in: R. D. Bergeron, A. E. Kaufman (Eds.), Proceedings of Visualization '94, IEEE, 1994, pp. 140 – 148.
44. I. J. LeGrice, Y. Takayama, J. W. Covell, Transverse shear along myocardial cleavage planes provides a mechanism for normal systolic wall thickening, Circulation Research 77 (1) (1995) 182–193.
45. S. Dokos, I. J. LeGrice, B. H. Smaill, J. Kar, A. A. Young, A triaxial-measurement shear-test device for soft biological tissue, Journal of Biomechanical Engineering 122 (5) (2000) 471–478.
46. S. Dokos, B. H. Smail, A. A. Young, I. J. LeGrice, Shear properties of passive ventricular myocardium, American Journal of Physiology 283 (6) (2002) H2650–H2659.
47. Y. Lavin, Y. Levy, L. Hesselink, Singularities in nonuniform tensor fields, in: R. Yagel,

H. Hagen (Eds.), Proceedings of Visualization '97, IEEE, 1997, pp. 59 – 66.
48. F. B. Sachse, C. Henriquez, G. Seemann, C. Riedel, C. D. Werner, R. C. Penland, B. Davis, E. Hsu, Modeling of fiber orientation in the ventricular myocardium with MR diffusion imaging, in: Proceedings of Computers in Cardiology, Vol. 28, 2001, pp. 617–620.
49. E. McVeigh, O. Faris, D. Ennis, P. Helm, F. Evans, Measurement of ventricular wall motion, epicardial electrical mapping and myocardial fiber angles in the same heart, in: T. Katila, I. E. Magnin, P. Clarysse, J. Montagnat, J. Nenonen (Eds.), Proceedings of the First International Workshop on Functional Imaging and Modeling of the Heart, Vol. 2230 of Lecture Notes in Computer Science, Springer, 2001, pp. 76–82.
50. T. Arts, K. D. Costa, J. W. Covell, A. D. McCulloch, Relating myocardial laminar architecture to shear strain and muscle fiber orientation, American Journal of Physiology 280 (5) (2001) H2222 – H2229.
51. T. D. Ruddy, R. A. deKamp, R. S. Beanlands, Taking PET to heart, eCMAJ - Canadian Medical Association Journal, Electronic Edition 161 (9).